Active Region Design With Different Crystal Orientations for High-Speed DFB Laser

Jianwei Li , Feng Gao , and Jia Zhao

Abstract—High-speed directly modulated distributed feedback (DFB) laser is crucial for high-speed optical communication systems. The modulation bandwidth and frequency chirp of such devices are primarily affected by the differential gain and linewidth enhancement factor (LEF) of the quantum wells (QWs) in the active region. In this work, the optical gain properties of long wavelength AlGaInAs-InP strained quantum wells (QWs) with different crystal orientations are numerically investigated using the multi-bands k.p theory, which considers both valence-band anisotropic and nonparabolicity. Compared to the QW laser grown on a conventional (001) substrate, a higher differential gain, and smaller LEF are observed for the laser grown on the (110) substrate with the $(\bar{1}10)$ plane as the mirror facet. This is primarily due to the reduced effective mass of the valence band. The dynamic characteristics of (001)-and (110)-oriented DFB laser is theoretically studied using the one-dimensional traveling wave model (1D TWM) at 25 °C and 95 °C. The simulation results show that the lower chirp and wider modulation bandwidth can be achieved for the QW laser grown on (110) substrate.

Index Terms—Crystal orientation, differential gain, linewidth enhancement factor, –3 dB bandwidth.

I. INTRODUCTION

HIGH-SPEED directly modulated quantum well-distributed feedback (DFB) lasers are the crucial components for high-speed optical communication systems, including fiber-optic networks and optical interconnects in data centers [1], [2]. Compared to external modulation techniques like Mach–Zehnder modulators and electro-absorption modulator integrated lasers (EML) [3], [4], directly modulated lasers (DMLs) generate optical signals with improved power efficiency and compact integration [5], [6]. However, the modulation bandwidth of DMLs is typically limited to around 30 GHz [7], [8] which could not meet the requirement for increasing network traffic. On the other hand, the maximum transmission distance and transmission bit rate are hugely restricted by the chirp-induced dispersion when the DFB laser is employed for standard single-mode fiber (SSMF) transmission [9], [10].

The modulation bandwidth of the DFB laser is primarily constrained by the intrinsic limitation posed by the quantum wells differential gain in the active region, which restricts how quickly the resonance frequency and damping of the resonant carrier-photon interaction can increase with the current. Increased differential gain results in a faster rise in resonance frequency, thereby enabling the DFB to achieve a greater modulation bandwidth before encountering damping limitations. The linewidth enhancement factor (LEF) is an important high-speed parameter in controlling frequency chirp effects. It is primarily influenced by the quantum well differential gain and the change of refractive index [11], [12]. Enhancing the differential gain can potentially decrease the linewidth enhancement factor and thus the chirp parameter. Over the years, many studies have focused on improving the differential gain at 1.3 μm and 1.55 μm by applying strained multiple quantum wells (MQW) composed of III-V materials such as InGaAsP and AlGaInAs [7]. Since 2000, the methods used for improving the differential gain of the quantum wells (QWs) in the active region have been quite restricted. Recent studies have shown that the energy band structure of III-V semiconductor materials is greatly affected by the orientation of the substrate, especially the valence band [13]. Therefore, the growing crystal orientations of the quantum well are considered to improve the quantum well differential gain and reduce the LEF. Till now, the optical properties of various crystal orientations have been investigated in different applications [14], [15], [16]. The effect of biaxial tensile strain on photoluminescence and carrier distribution with differently oriented germanium (Ge) has been studied in previous research [17]. Atsuko Niwa et al. have theoretically calculated the Linewidth enhancement factor for InGaAs/InGaAsP QW with (11N)-orientation [18]. M.M. Hasana et al. realized the maximum optical power and minimum threshold current by optimizing the GaInSb QW Mid-infrared lasers in (113) crystal orientation [19]. Hosni Saidi theoretically reported the impact of piezoelectricity on the optical transition and gain within a quantum well (QW) composed of [111]-oriented GaAs/InGaAs [20].

The growth of high-quality quantum well epitaxial layers on different orientation substrates poses a great challenge to the crystal growers due to the difference in growth kinetics on non-(001) oriented substrates, such as the growth rate, ambient temperature, and strain corresponding to different quantum well material systems [21]. Fortunately, with the advancement of growth techniques, high-quality quantum well growth on crystal orientations (111), (110), (311), (411), (511), (118) have been

realized by optimizing crystal growth conditions using Molecular Beam Epitaxy (MBE), and Metal-Organic Chemical Vapor Deposition (MOCVD) epitaxial growth technique [22], [23], [24], [25], [26].

In this article, we investigate the influences of differential gain and linewidth enhancement factor (LEF) on the direct modulation characteristics of AlGaInAs/InP compressive strained (CS) QW DFB lasers with different substrate orientations. The Hamiltonian for arbitrary crystal orientations is derived by applying a spinor rotation to the (001)-oriented Hamiltonian. Based on the accurate energy band calculation using the finite-difference procedures, we carefully analyze the optical gain, differential gain, and LEF in different crystal orientations. We observe that the gain and differential gain can be enhanced by growing on a non-(001) orientation QW compared to the conventional (001) oriented QW. Then, the dynamic behaviors of the DFB lasers on (001) and (110) orientations are separately calculated. The high modulation bandwidth and lower chirp are realized for the (110) substrate QW DFB laser, which can support the higher modulation speeds.

This paper is structured as follows: Section II provides the simulation model and parameters for arbitrary crystal orientation. In Section III, the results for arbitrary crystal-oriented MQW gain, differential gain, and LEF are discussed. The dynamic response of the DFB laser is shown as well. The conclusion is summarized in Section IV.

II. MQW DFB LASER MODEL

A. MQW Gain Model for Different Orientations

The (001) Hamiltonian for QW valence bands is used by 4×4 band luttinger-Khon matrices, which include the biaxial strain [27]:

$$H^{(001)} = - \begin{bmatrix} P+Q & -S & R & 0 \\ -S^\dagger & P-Q & 0 & S \\ R^\dagger & 0 & P-Q & S \\ 0 & R^\dagger & S^\dagger & P+Q \end{bmatrix} \quad (1)$$

Replacing k_z in above Hamiltonian $H^{(001)}$ with the operator $-i\partial/\partial z$ yields the quantum well matrix elements P, Q, R, and S as [28]:

$$P = \frac{\hbar^2\gamma_1}{2m_0}\left(k_x^2 + k_y^2 - \frac{\partial^2}{\partial z^2}\right) - a_v(\varepsilon_{xx} + \varepsilon_{yy} + \varepsilon_{zz}), \quad (2)$$

$$Q = \frac{\hbar^2\gamma_2}{2m_0}\left(k_x^2 + k_y^2 + 2\frac{\partial^2}{\partial z^2}\right) - \frac{b}{2}(\varepsilon_{xx} + \varepsilon_{yy} - 2\varepsilon_{zz}), \quad (3)$$

$$R = \frac{\hbar^2}{2m_0}$$
$$\left[-\sqrt{3}\gamma_2(k_x^2-k_y^2)+i2\sqrt{3}k_xk_y+\frac{\sqrt{3}}{2}b(\varepsilon_{xx}-\varepsilon_{yy})-\sqrt{3}id\varepsilon_{xy}\right], \quad (4)$$

$$S = \frac{\hbar^2\gamma_3}{2m_0}\sqrt{3}(ik_x + k_y)\frac{\partial}{\partial z} - \sqrt{3}d(\varepsilon_{xz} - i\varepsilon_{yz}), \quad (5)$$

where m_0 is the electron mass. $k_i(i = x, y, z)$ are wave vectors. ε_{ij} are the strain tensors. The $\gamma_{1,2,3}$ are labeled as Luttinger parameters while a_v, b, and d are the valence band hydrostatic deformation and shear deformation potentials, respectively. The Hamiltonians with different orientations are derived by rotating the (001) Hamiltonian $H^{(001)}$ mentioned above. [29]:

$$H^{(hkl)} = UH^{(001)}U^*, \quad (6)$$

here, U represents spinor rotations for angular momentum $J = 3/2$, denoted as $R_{y'}(\theta)$ and $R_z(\phi)$, which converts the Hamiltonian of the valence band from (001) substrate orientation to different crystal orientations. The wave vectors k_i' and the strain tensors $\varepsilon_{i,j}'$ that correspond to different crystal orientations can be derived employing the rotation matrix [30]:

$$T_R = \begin{pmatrix} \cos(\theta)\cos(\phi) & -\sin(\phi) & \sin(\theta)\cos(\phi) \\ \cos(\theta)\sin(\phi) & \cos(\phi) & \sin(\theta)\sin(\phi) \\ -\sin(\theta) & 0 & \cos(\theta) \end{pmatrix}. \quad (7)$$

Here, $\phi = \arctan(\sqrt{h^2 + k^2}/l), \theta = \arctan(k/h)$, h, k, l are the Miller indexes. The valence sub-band energy dispersion for a QW grown with different orientations can be determined by solving:

$$\left[H^{(hkl)} + V_h(z')\right]\psi_h(z') = E\psi_h(z'). \quad (8)$$

In the case of conduction bands, where electron effective mass is virtually isotropic, and the electron eigenfunctions exhibit spherical symmetry, we employ the single-band Hamiltonian [15], [31]:

$$H^c(k) = \frac{\hbar^2}{2}\left(\frac{k_x'^2 + k_y'^2}{m_e^*(z')} + \frac{1}{m_e^*(z')}\left(-\frac{\partial^2}{\partial z'^2}\right)\right) + V_e(z')$$
$$+ a_c(\varepsilon'_{xx} + \varepsilon'_{yy} + \varepsilon'_{zz}), \quad (9)$$

where $m_e^*(z')$ is the conduction band electron-effective mass. $V_e(z')$ is the conduction band edge energies for the unstrained quantum well. a_c referred to as conduction-band hydrostatic deformation.

The optical gain expression for the multi-quantum well architecture that involves valence band anisotropic and mixing effects can be expressed as follows: [32]:

$$g(\hbar\omega) = \frac{q^2\pi}{n_r c\epsilon_0 m_0^2\omega}\sum_{n,m}\int_0^{k_{max}}\frac{2k_\parallel}{(2\pi)^2 L_w}dk_\parallel$$
$$\times \int_0^{2\pi}d\varphi_0|\hat{e}\cdot M_{n,m}(k_\parallel,\varphi_0)|^2$$
$$\times \frac{(f_c^n(k_\parallel,\varphi_0) - f_v^m(k_\parallel,\varphi_0))\gamma/\pi}{(E_{c,v}^{n,m}(k_\parallel,\varphi_0) - \hbar\omega)^2 + \gamma^2}, \quad (10)$$

where

$$f_c^n(k_\parallel,\varphi_0) = \left[1 + exp\left[\frac{E_c^n(k_\parallel,\varphi_0) - F_c}{K_BT}\right]\right]^2, \quad (11)$$

$$f_v^m(k_\parallel,\varphi_0) = \left[1 + exp\left[\frac{E_v^m(k_\parallel,\varphi_0) - F_v}{K_BT}\right]\right]^2, \quad (12)$$

$$E_{c,v}^{n,m}\left(k_{\parallel},\varphi_0\right) = E_c^n\left(k_{\parallel},\varphi_0\right) - E_v^m\left(k_{\parallel},\varphi_0\right), \qquad (13)$$

The angle and magnitude of the wave vector in the QW plane are represented by φ_0 and $k_{\parallel}$, respectively. q represents the elementary charge, ϵ_0 stands for permittivity in free space, L_w signifies the width of the quantum well, and n_r denotes refractive index. $|\hat{e} \cdot M_{n,m}(k_{\parallel},\varphi_0)|$ represents the transition momentum matrix elements and $\hat{e}$ is the polarization direction. We assume that the intraband relaxation time γ^{-1} is 0.1ps. The summation of the electron spins is explicitly included in (10).

The variations in carrier density simultaneously influence the gain and refractive index. Refractive index change can be expressed as $\Delta n_r = \Delta\epsilon_1/(2n_r\epsilon_0)$, where the factor $\Delta\epsilon_1/\epsilon_0$ of can be obtained by:

$$\frac{\Delta\epsilon_1\left(\hbar\omega\right)}{\epsilon_0} = \frac{2q^2\hbar}{m_0^2\epsilon_0 L_w} \sum_{n,m} \int_0^{k_{\max}} \frac{2k_{\parallel}}{(2\pi)^2} dk_{\parallel}$$

$$\times \int_0^{2\pi} d\varphi_0 \left|\hat{e} \cdot M_{n,m}\left(k_{\parallel},\varphi_0\right)\right|^2$$

$$\times \frac{\left(E_{c,v}^{n,m}\left(k_{\parallel},\varphi_0\right) - \hbar\omega\right)}{E_{c,v}^{n,m}\left(k_{\parallel},\varphi_0\right)\left(E_{c,v}^{n,m}\left(k_{\parallel},\varphi_0\right) + \hbar\omega\right)}$$

$$\times \frac{f_v^m\left(k_{\parallel},\varphi_0\right) - f_c^n\left(k_{\parallel},\varphi_0\right)}{\left(E_{c,v}^{n,m}\left(k_{\parallel},\varphi_0\right) - \hbar\omega\right)^2 + \gamma^2}. \qquad (14)$$

The linewidth enhancement factor (LEF) is a crucial parameter influencing the laser linewidth, which is important for high-speed applications. It can be determined by [33]:

$$\alpha_{LEF} = -\frac{4\pi}{\lambda_0}\frac{\partial\Delta n_r/\partial N}{\partial g/\partial N}, \qquad (15)$$

here the denominator $\partial g/\partial N$ represents the differential gain, while the numerator $\partial\Delta n_r/\partial N$ signifies the change in the effective refractive index resulting from carrier injection.

In this research, we employ linear interpolation to derive the relevant parameter for $Al_yGa_xIn_{1-x-y}As$ material systems based on the parameters of the related binary semiconductors, The interpolation formulae are as follows:

$$P\left(Al_yGa_xIn_{1-x-y}As\right) = x \cdot P\left(GaAs\right) + y \cdot P\left(AlAs\right)$$
$$+ (1-x-y) \cdot P\left(InAs\right), \quad (16)$$

the material parameters used in the modeling are sourced from [34], and the temperature-dependent bandgap energy is calculated using the following expression [35]:

$$Eg\left(Al_yGa_xIn_{1-x-y}As\right)$$
$$= 0.360 + x \cdot 0.629 + y \cdot 2.039$$
$$+ x^2 \cdot 0.436 + y^2 \cdot 0.577 + x \cdot y$$
$$\cdot 1.013 - 4.1 \times 10^{-4} \cdot \left[\frac{T^2}{T+136} - \frac{300^2}{300+136}\right] (eV).$$
$$(17)$$

B. Dynamic Modeling of DFB Laser

The dynamic properties of DFB lasers can be simulated by the 1D traveling wave model (TWM) [36], [37]:

$$\frac{1}{v_g}\frac{\partial F\left(z,t\right)}{\partial t} + \frac{\partial F\left(z,t\right)}{\partial z}$$
$$= \left\{\frac{\Gamma G\left(z,t\right)}{2\left(1+\varepsilon P^s\left(z,t\right)\right)} - \frac{1}{2}\alpha - j\delta\right\}$$
$$\cdot F\left(z,t\right) + j\kappa R\left(z,t\right) + \tilde{s}^f\left(z,t\right), \qquad (18)$$

$$\frac{1}{v_g}\frac{\partial R\left(z,t\right)}{\partial t} - \frac{\partial R\left(z,t\right)}{\partial z} = \left\{\frac{\Gamma G\left(z,t\right)}{2\left(1+\varepsilon P^s\left(z,t\right)\right)} - \frac{1}{2}\alpha - j\delta\right\}$$
$$\cdot R\left(z,t\right) + j\kappa F\left(z,t\right) + \tilde{s}^r\left(z,t\right), \qquad (19)$$

where F and R represent the traveling optical fields for forward and backward propagating waves within the resonant cavity. α is the internal loss P^s is the photon density distribution, ε nonlinear gain suppression coefficient, κ is the grating coupling coefficient, and $\tilde{s}^f$, $\tilde{s}^r$ represent Gaussian-distributed spontaneous emission noise fields, δ is the phase detuning and is written as $\delta = [2\pi n_{eff}^0/\lambda_0 - 1/2\alpha_{LEF}\Gamma G(z,t) - \pi/\Lambda]$. For the quantum well active region, the modal gain g_m can be well approximated by the logarithmic function:

$$g_m\left(z,t\right) = \Gamma G\left(z,t\right) = \Gamma g_0 \, ln\left(\frac{N\left(z,t\right)}{N_{tr}}\right), \qquad (20)$$

where the g_0 is gain constant and N_{tr} is transparent carrier density, Γ is the optical confinement factor for MQW. The carrier density N can be solved using the rate equation:

$$\frac{dN\left(z,t\right)}{dt} = \eta\frac{I\left(t\right)}{eV} - \frac{N}{\tau_n} - \frac{v_g P^s\left(z,t\right) g\left(z,t\right)}{1+\varepsilon P_s\left(z,t\right)}, \qquad (21)$$

where $I(t)$ represents the injected current, V is the volume of the active region, $v_g = c/n_g$ is the group velocity, n_g the group index, and τ_n the carrier lifetime.

III. SIMULATION RESULTS AND DISCUSSIONS

In this segment, in order to achieve the gain peak close to 1.3 μm wavelength range, the crystal orientation-dependent optical properties for $Al_{0.1}Ga_{0.23}In_{0.67}As/Al_{0.5}Ga_{0.12}In_{0.38}As$ strained QW with $L_w = 5$ nm are calculated. A barrier width of 10 nm is adopted, which is large enough to eliminate the coupling of MQW. So, the valence band energy $E_m^v(k)$ in the k_z direction can be negligible as described in [38]. The valence bands for (001), (111), (110), and (538) oriented QWs are displayed in Fig. 1(a)–(d), respectively. In Fig. 1, The split energy between HH1 and HH2 for the four orientations is separately 0.0801 eV, 0.0444 eV, 0.0636 eV, and 0.06319 eV, which reveals the relative differences in the position of sub-bands. Fig. 1(a) and (b) illustrate that in the case of the (001) oriented quantum well (QW), the band structure exhibits an approximate symmetry along the in-plane [100] and [110] directions and in-plane [11$\bar{2}$] and [$\bar{1}$10] directions for (111)-oriented QWs. Fig. 1(c) and (d) show the anisotropy of the structure of the (110) and (538)
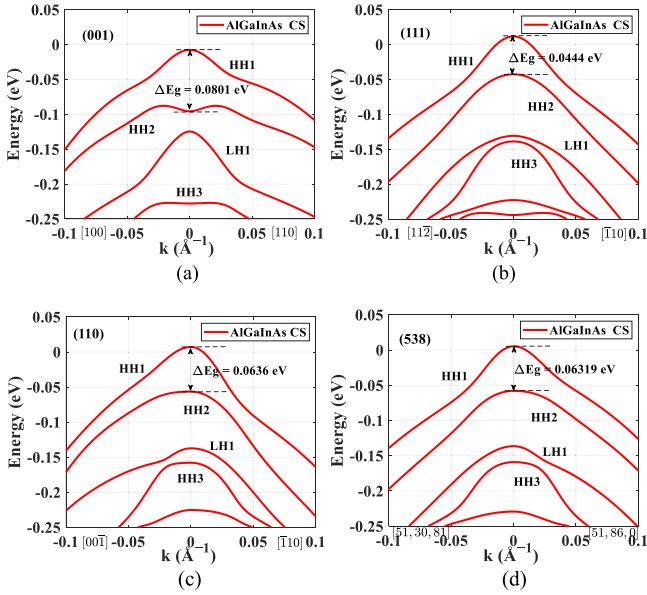
Fig. 1. Energy band dispersion profile of 0.95% compressively strained InAlGaAs QW laser in (a) (001), (b) (111), (c) (110), and (d) (538) orientation.
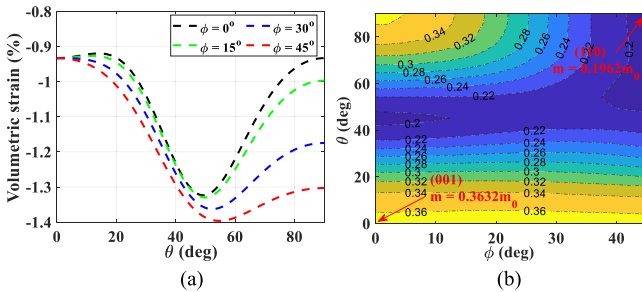

Fig. 2. (a) Volumetrical strains caused by biaxial stress and (b) effective mass as a function of θ and ϕ.
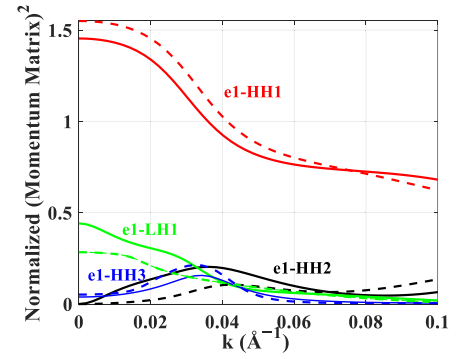

Fig. 3. Normalized momentum matrix elements for (001) (solid line)- and (110) (dashed line)-oriented QWs.
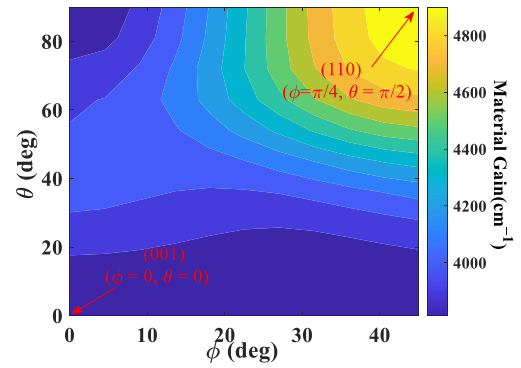

Fig. 4. Peak gain of quantum well as a function of the polar angle θ and azimuthal angle ϕ at the carrier density $N = 5 \times 10^{18}$ cm^{-3}.

oriented QW bands. As a result, the E-k dispersion curves are significantly influenced by both the growth direction and the in-plane direction, resulting in distinct in-plane effective masses, which further affect the optical properties.

Fig. 2(a) shows the calculated volumetric strain $\varepsilon'_{xx} + \varepsilon'_{yy} + \varepsilon'_{zz}$ for different angles of θ and ϕ, which determines the QWs orientations. It's important to highlight that the energy shift induced by strain, as described in (9), is directly proportional to the volumetric strain. and the value reaches the maximum for the $(\theta = \arccos(1/\sqrt{3}), \phi = \pi/4)$(111)-oriented QWs. Fig. 2(b) shows the valence band effective mass for different orientations near the Brillouin Center. It can be seen that the effective mass of these QWs is dependent on growth orientation. The effective mass of heavy holes for (001) $(\theta = 0, \phi = 0)$ orientation is $0.3632m_0$. However, the effective mass for the (538) $(\theta \approx 0.5404, \phi \approx 0.6298)$, (111) $(\theta = \arccos(1/\sqrt{3}), \phi = \pi/4)$ and (110) $(\theta = \pi/2, \phi = \pi/4)$-oriented QWs are $0.2405m_0$, $0.1957m_0$ and $0.1962m_0$, respectively. Therefore, the reduction in the effective mass of the valence band in (110) and (111)-oriented quantum wells effectively

diminishes the asymmetry with the conduction band, resulting in higher differential gain and lower transparency carrier density.

Fig. 3 presents the normalized momentum matrix elements of TE polarizations for (001) (solid line)- and (110) (dashed line)-oriented QWs for the e1-HH1, e1-LH1, e1-HH2, and e1-HH3 transitions. We can observe that in the (110)-oriented QW, the momentum matrix elements e1-HH1 parallel to $[\bar{1}10]$ direction is greater than the momentum matrix element in the (001) oriented QW due to the anisotropy of valence sub-bands as shown in Fig. 1.

Fig. 4 calculates the peak gain as a function of the polar angle θ and azimuthal angle ϕ at the carrier density $N = 5 \times 10^{18}$ cm^{-3}. We find that the peak material gains are 3772 cm^{-1}, 4965 cm^{-1}, 4017 cm^{-1} and 4602 cm^{-1}, respectively, for the (001), (110), (538) and (111)-oriented QWs. In other orientations, we find the peak gain is isotropic when $\theta = 0$. The largest peak gain is in (110)-oriented QW. It is shown that the (110) orientation QW with the $(\bar{1}10)$ plane as the mirror facet is the best for edge-emitting lasers.

The quantum well material gain and the differential gain spectra in (001) and (110) orientations QW are separately shown in Fig. 5(a) and (b) with the threshold gain $g_{th} = 500$ cm^{-1}. The red (green) curves represent the TE(TM) gain and differential gain spectra, respectively, with the TE gain being greater than the TM gain. Furthermore, it was found that, at the wavelength of 1310 nm, the differential gain with (110) orientation exceeds that of the (001)-oriented quantum well by a factor of 1.713. In
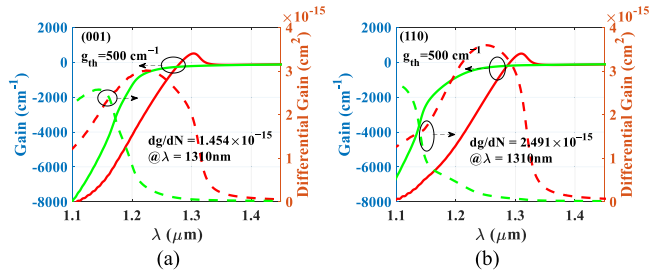
Fig. 5. Material gain spectra and the differential gain for (a) (001) and (b) (110) orientation QW when $g_{th} = 500$ cm^{-1}. The red line is TE modes, and the green line is TM modes.

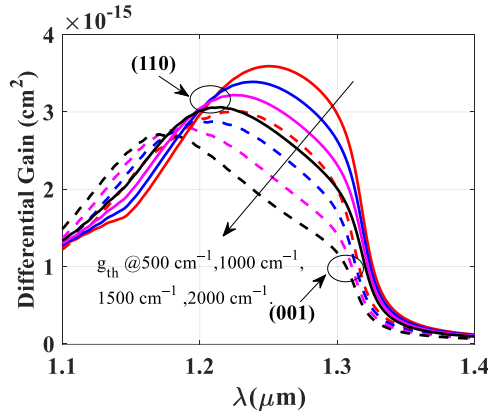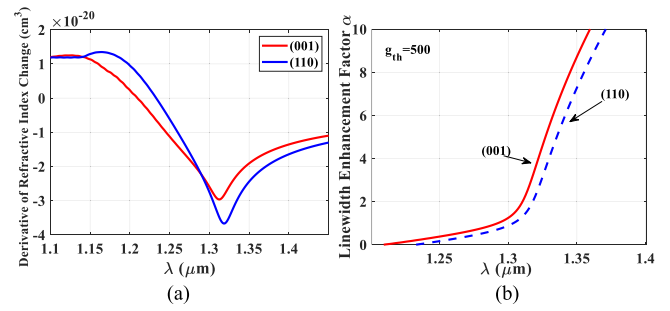Fig. 7. (a) Graph of the derivative of the change in refractive index concerning carrier density versus wavelength (b) graph of the LEF versus wavelength.
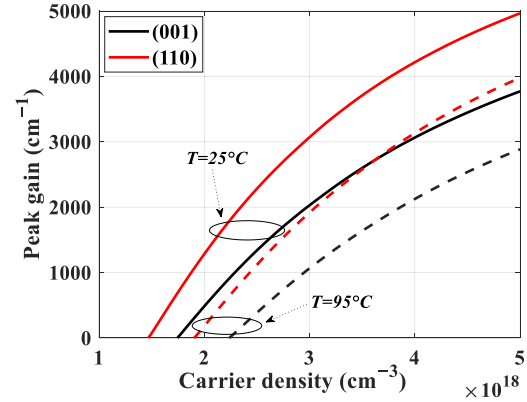

Fig. 6. Differential gain spectra for (110) and (001) orientation quantum wells are shown at various threshold gains.

Fig. 8. Peak material gain concerning carrier density at 25 °C and 95 °C with (001), and (110)-orientation QWs.

addition, Fig. 5(a) illustrates that the differential gain of (001)-oriented QW has a peak at approximately 1.22 μm. Regarding the (110)-oriented QWs, Fig. 5(b) reveals the peak is 1.252 μm, significantly distant from the laser wavelength. Shifting the peak of the differential gain spectrum into the positive gain region could lead to substantial enhancements in (DFB) laser characteristics.

As shown in Fig. 6, the differential gain for different crystal orientations at threshold gains of 500 cm^{-1}, 1000 cm^{-1}, 1500 cm^{-1}, and 2000 cm^{-1}. the shape of differential gain spectra becomes flat with increasing threshold gain. However, compared to the (001) crystal orientation, the peaks of the differential gain spectra in (110)-oriented quantum wells shift towards the longer wavelength, and largely enhanced peak values are observed in (110)-oriented quantum well at various threshold gains.

Fig. 7(a) displays the variation in the refractive index due to changes in carrier density. The most significant change occurs as the photon energy approaches the transition energy. The (001)-oriented QWs have a smaller valve compared with that of (110)-oriented QWs with the wavelength larger than 1290 nm. Fig. 7(b) shows the LEF for strained (001)- and (110)-oriented QW lasers with the threshold gain of 500 cm^{-1}. A smaller LEF of 1.27 is realized for the (110)-oriented QW lasers while the LEF in the (001) case is 1.963 with the wavelength of 1310 nm. Furthermore, we find that the LEF rises rapidly with wavelength increasing, especially with a wavelength larger than 1320 nm. By combining it with additional methods like p-type doping [39]

TABLE I
DIFFERENTIAL GAIN AT TRANSPARENCY CARRIER DENSITY

Crystal orientation	Gain coefficient g_0 (cm^{-1})	Transparency carrier density N_{tr} (10^{18} cm^{-3})	Differential gain (10^{-15} cm^2)
(001)	3603.2	1.72	2.0949
	(3545.4)	(2.22)	(1.5968)
(110)	4225.2	1.48	2.8549
	(4176.6)	(1.90)	(2.1982)

Numbers in parenthesis are at 95°C, others at 25°C.

and wavelength detuning [40], further reduction of this value can be achieved.

The peak material gain at 25 °C and 95 °C with orientations of (001), and (110) is depicted in Fig. 8 concerning carrier density. The transparency carrier density simulated at 25 °C decreases from 1.72×10^{18} cm^{-3} to 1.48×10^{18} cm^{-3} as the QW orientation is changed from (001) to (110). The (110)-oriented QW has the higher differential gain at a low carrier density. In addition, both the peak gain and transparency carrier density at 95 °C show similar trends as observed at 25°C. Next, the logarithmic function (20) is used to fit the transparency carrier densities and the gain coefficient for (110)- and (001)-oriented QW. The corresponding differential gain is also shown. The results are summarized in Table I.
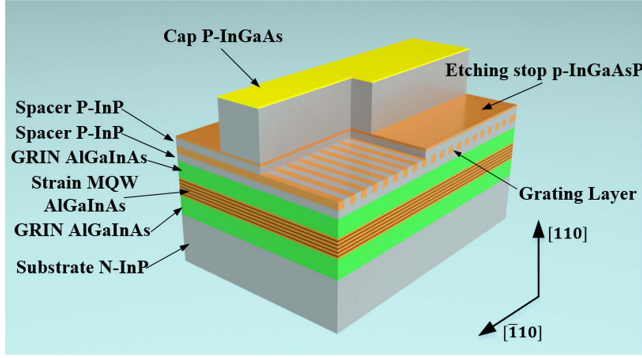
Fig. 9. 3D schematic diagram of the (110) orientation QW DFB laser.

TABLE II
SIMULATION PARAMETERS FOR DFB LASER

Parameters	Symbol (unit)	Value
Cavity length	$L(\mu m)$	200
Active region thickness	$d(nm)$	55
Grating coupling coefficient	$\kappa(cm^{-1})$	110
Carrier lifetime	$\tau_n(ns)$	0.8
Optical Confinement factor	Γ	0.1
Internal loss	$\alpha(cm^{-1})$	10
Linewidth enhancement factor	α_{LEF}	1.27, 1.963
Reflectivity of front facet	R_f	0.005
Reflectivity of rear facet	R_r	0.95
Effective index without injection	n_{neff}	3.226
Grating period	$\Lambda(nm)$	203.0
Nonlinear gain saturation coefficient	$\varepsilon(10^{-17}cm^3)$	2
Current injection efficiency	η	1

By optimizing the gain properties of QWs in the active region as shown in Table I, a schematic drawing of the (110) orientation strained InAlGaAs MQW DFB laser is presented in Fig. 9, with the ($\bar{1}$10) plane as the mirror facet. The active region employs eleven 5 nm-thick MQW structures, which reduces the threshold current and increases the output optical power for high-speed modulation applications. The wells are separated by large barrier width so that the MQW coupling effects can be negligible assuming the material gain is the same for each QW [41]. The other parameters used for the dynamic response simulation of the DFB laser are listed in Table II.

The small-signal modulation responses at 25 °C and 95 °C are shown in Fig. 10(a)–(b) for (001)-and (110)-oriented QW DFB laser. With the injection current increasing, the –3 dB bandwidth is elevated due to the higher photon density. We observe that the (110)-oriented QW laser displays higher modulation bandwidth. Compared with that of (001)-oriented QW laser, the –3 dB bandwidth increases from 20.75 Ghz to 25.25 Ghz at 25 °C and from 18.55 Ghz to 22.54 Ghz at 95 °C at an injection current of 40 mA.
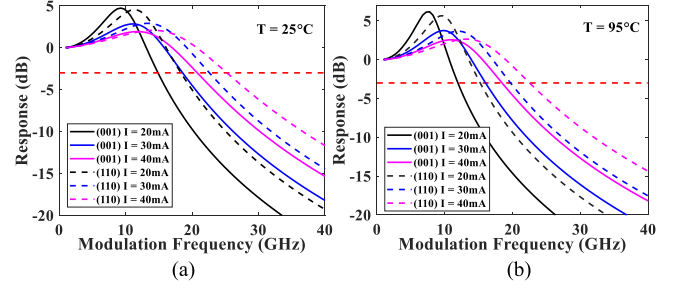

Fig. 10. Small-signal response for the (001) (solid line)- and (110) (dashed line) orientation QW DFB laser at (a) 25 °C and (b) 95 °C.
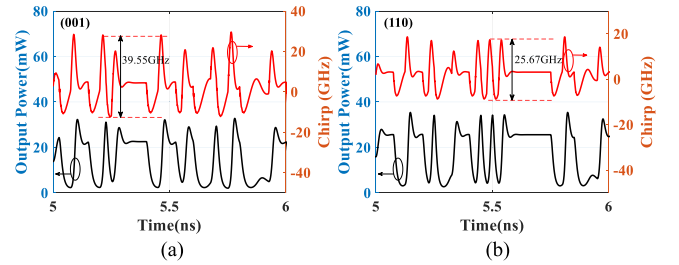

Fig. 11. Time-varying characteristics of modulated laser power and frequency chirp at 40 Gbps NRZ modulation for the (a) (001) and (b) (110) orientation.
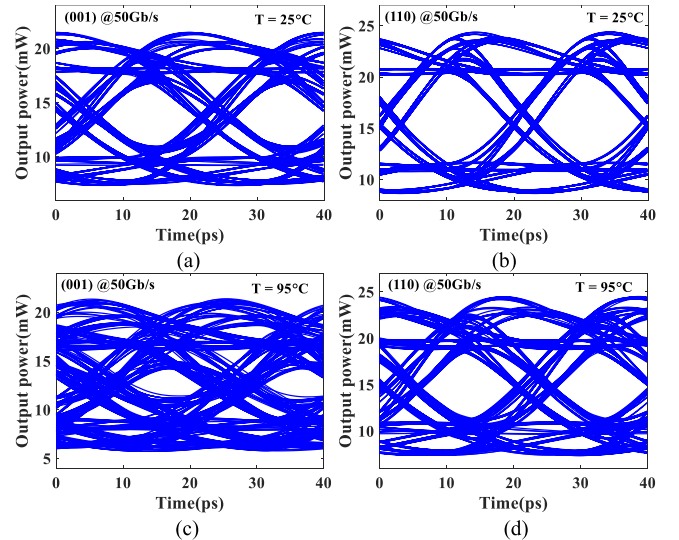

Fig. 12. Non-return-to-zero (NRZ) eye diagram of (001) and (110) QWs DFB laser modulated at 50 Gb/s for bias of 40 ± 10 mA at (a) and (b) 25 °C and (c) and (d) 95 °C.

Fig. 11 shows the modulated laser output power and the associated frequency chirp at 40 Gbps using a non-return-to-zero (NRZ) modulation format. The peak-to-peak chirps are 39.55 GHz and 25.67 GHz, respectively, for the (001) orientation and (110) orientation devices. Fig. 12 shows the (NRZ) eye diagram of (001) and (110) QWs DFB laser at 50Gb/s with an injection current of 40 ± 10 mA at 25 °C and 95 °C. We can find that the (110)-oriented QWs DFB laser can largely improve the optical eye-opening, and thus achieve error-free bit rate transmission.

IV. Conclusion

In summary, the optical gain and dynamic properties of the compressively strained AlGaInAs QW DFB laser grown on an InP substrate with arbitrary orientation are analyzed theoretically. We have performed a detailed analysis of the band structure, effective mass, momentum matrix elements, optical gain, differential gain, and LEF. Our results show that (110)-oriented QWs with the $(\bar{1}10)$ plane as the mirror facet is the most promising for high-speed DFB laser. In contrast to the (001)-oriented quantum well, the (110)-oriented quantum well exhibits higher optical differential gain and lower transparency carrier density. The small-signal modulation responses show a good 3 dB bandwidth from 20.75 GHz to 25.25 GHz at $25\,^\circ\text{C}$ and from 18.55 GHz to 22.54 GHz at $95\,^\circ\text{C}$ for the 40 mA bias level. In addition, the peak-to-peak chirp of the (110) orientation is lower than the (001) case at 40 Gbps NRZ modulation. The present research findings provide new degrees of freedom for enhancing the quantum well differential gain and reducing the linewidth enhancement factor (LEF) of photonic devices.

Acknowledgment

References

[1] N. H. Zhu et al., "Directly modulated semiconductor lasers," *IEEE J. Sel. Topics Quantum Electron.*, vol. 24, no. 1, pp. 1–19, Jan./Feb. 2018, doi: 10.1109/JSTQE.2017.2720959.

[2] T. Sudo et al., "Challenges and opportunities in directly modulated lasers in future data center and 5G networks," in *Proc. Opt. Fiber Commun.*, 2021, Paper Tu1B.3.

[3] S. Kanazawa et al., "214-Gb/s 4-PAM operation of flip-chip interconnection EADFB laser module," *J. Lightw. Technol.*, vol. 35, no. 3, pp. 418–422, Feb. 2017, doi: 10.1109/JLT.2016.2632164.

[4] S. Lange et al., "100 GBd intensity modulation and direct detection with an InP-based monolithic DFB laser Mach–Zehnder modulator," *J. Lightw. Technol.*, vol. 36, no. 1, pp. 97–102, Jan. 2018, doi: 10.1109/JLT.2017.2743211.

[5] S. Matsuo and T. Kakitsuka, "Low-operating-energy directly modulated lasers for short-distance optical interconnects," *Adv. Opt. Photon.*, vol. 10, no. 3, Sep. 2018, Art. no. 567, doi: 10.1364/AOP.10.000567.

[6] J. Huang, C. Li, R. Lu, L. Li, and Z. Cao, "Beyond the 100 gbaud directly modulated laser for short reach applications," *J. Semicond.*, vol. 42, no. 4, Apr. 2021, Art. no. 041306, doi: 10.1088/1674-4926/42/4/041306.

[7] S. Yamaoka et al., "Directly modulated membrane lasers with 108 GHz bandwidth on a high-thermal-conductivity silicon carbide substrate," *Nature Photon.*, vol. 15, no. 1, pp. 28–35, Jan. 2021, doi: 10.1038/s41566-020-00700-y.

[8] D. Che et al., "Direct modulation of a 54-GHz distributed Bragg reflector laser with 100-GBaud PAM-4 and 80-GBaud PAM-8," in *Proc. Opt. Fiber Commun.*, 2020, Paper Th3C.1.

[9] G. Liu, G. Zhao, G. Zhang, Y. Liu, Q. Lu, and W. Guo, "Experimental demonstration of directly modulated DFB lasers with negative chirp over wide temperature operation," *J. Lightw. Technol.*, vol. 38, no. 14, pp. 3663–3669, Jul. 2020, doi: 10.1109/JLT.2020.2979337.

[10] Y. Matsui, R. Schatz, D. Che, F. Khan, M. Kwakernaak, and T. Sudo, "Low-chirp isolator-free 65-GHz-bandwidth directly modulated lasers," *Nature Photon.*, vol. 15, no. 1, pp. 59–63, Jan. 2021, doi: 10.1038/s41566-020-00742-2.

[11] A. Mahmoud, N. Fouad, M. Ahmed, and T. Mohamed, "Effect of linewidth enhancement factor of laser diode and fiber dispersion management on high-speed optical fiber links performance and use in WDM systems," *Opt. Quantum Electron.*, vol. 55, no. 2, Feb. 2023, Art. no. 158, doi: 10.1007/s11082-022-04379-z.

[12] N. Fouad, T. Mohamed, and A. Mahmoud, "Impact of linewidth enhancement factor and gain suppression on chirp characteristics of high-speed laser diode and performance of 40 Gbps optical fiber links," *Appl. Phys. B*, vol. 128, no. 3, Mar. 2022, Art. no. 45, doi: 10.1007/s00340-022-07771-5.

[13] M. Gladysiewicz and M. S. Wartak, "Effect of substrate orientation on band structure of bulk III-V semiconductors," *AIP Adv.*, vol. 12, no. 11, Nov. 2022, Art. no. 115208, doi: 10.1063/5.0118226.

[14] S.-H. Park, D. Ahn, and S.-L. Chuang, "Electronic and optical properties of a - and m -plane wurtzite InGaN–GaN quantum wells," *IEEE J. Quantum Electron.*, vol. 43, no. 12, pp. 1175–1182, Dec. 2007, doi: 10.1109/JQE.2007.905009.

[15] S. Roy et al., "Numerical investigation into optical and electronic performance of crystal orientation-dependent InGaAs/InP near-infrared laser," *Results Phys.*, vol. 26, Jul. 2021, Art. no. 104353, doi: 10.1016/j.rinp.2021.104353.

[16] J. Li, J. Zhao, and F. Gao, "Numerical investigation of optical and photoelectric properties for 850 nm VCSELs with arbitrary crystal orientation," *Crystals*, vol. 12, no. 10, Oct. 2022, Art. no. 1459, doi: 10.3390/cryst12101459.

[17] G.-E. Chang and H. H. Cheng, "Optical gain of germanium infrared lasers on different crystal orientations," *J. Phys. D: Appl. Phys.*, vol. 46, no. 6, Feb. 2013, Art. no. 065103, doi: 10.1088/0022-3727/46/6/065103.

[18] T. Ohtoshi, T. Kuroda, A. Niwa, and S. Tsuji, "Dependence of linewidth enhancement factor on crystal orientation in strained quantum well lasers," *IEEE Photon. Technol. Lett.*, vol. 6, no. 12, pp. 1424–1426, Dec. 1994, doi: 10.1109/68.392223.

[19] M. M. Hasan, M. R. Islam, and K. Teramoto, "Crystallographic orientation-dependent optical properties of GaInSb mid-infrared quantum well laser," *Optik*, vol. 123, no. 21, pp. 1993–1997, Nov. 2012, doi: 10.1016/j.ijleo.2011.09.021.

[20] H. Saidi, O. Zitouni, and S. Ridene, "Investigation of orientation dependence of piezoelectric effects in strained GaAs/InGaAs quantum well laser," *Mater. Sci. Eng. B*, vol. 273, Nov. 2021, Art. no. 115400, doi: 10.1016/j.mseb.2021.115400.

[21] T. Hayakawa, M. Kondo, T. Suyama, K. Takahashi, S. Yamamoto, and T. Hijikata, "Reduction in threshold current density of quantum well lasers grown by molecular beam epitaxy on 0.5° misoriented (111)B substrates," *Jpn. J. Appl. Phys.*, vol. 26, no. 4A, Apr. 1987, Art. no. L302, doi: 10.1143/JJAP.26.L302.

[22] C. Caneau, R. Bhat, and N. Nishiyama, "Variation of the morphology of strained AlGaInAs quantum wells with substrate orientation," *J. Cryst. Growth*, vol. 310, no. 7–9, pp. 2345–2352, Apr. 2008, doi: 10.1016/j.jcrysgro.2007.11.002.

[23] Y. Yasuda, S. Koh, K. Ikeda, and H. Kawaguchi, "Crystal growth of InGaAs/InAlAs quantum wells on InP (110) by MBE," *J. Cryst. Growth*, vol. 364, pp. 95–100, Feb. 2013, doi: 10.1016/j.jcrysgro.2012.11.039.

[24] B. Smiri, F. Saidi, A. Mlayah, and H. Maaref, "Comparative optical studies of InAlAs/InP quantum wells grown by MOCVD on (311)A and (311)B InP planes," *J. Mater. Sci.: Mater. Electron.*, vol. 31, no. 13, pp. 10750–10759, Jul. 2020, doi: 10.1007/s10854-020-03625-y.

[25] T. Kitada et al., "Super-flat interfaces in $In_{0.53}Ga_{0.47}As/InAl_{0.48}As$ quantum wells grown on (411)A InP substrates by molecular beam epitaxy," *J. Electron. Mater.*, vol. 27, no. 9, pp. 1043–1046, Sep. 1998, doi: 10.1007/s11664-998-0161-9.

[26] T. J. Thornton, J. M. Fernández, S. Kaya, P. W. Green, and K. Fobelets, "Si:SiGe quantum wells grown on (118) substrates: Surface morphology and transport properties," *Appl. Phys. Lett.*, vol. 70, no. 10, pp. 1278–1280, Mar. 1997, doi: 10.1063/1.118526.

[27] J. Piprek, Ed., *Handbook of Optoelectronic Device Modeling and Simulation* (in Series in optics and optoelectronics). Boca Raton, FL, USA: CRC Press, 2018.

[28] S. Roy, M. Hassan, A. Karmaker, S. Poddar, and M. S. Hossain, "Strain-dependent optical properties of [113]-oriented InGaAs/GaAs quantum well," in *Proc. IEEE Int. Conf. Adv. Elect. Eng.*, 2015, pp. 340–343.

[29] T. Ohtoshi, T. Kuroda, A. Niwa, and S. Tsuji, "Dependence of optical gain on crystal orientation in surface-emitting lasers with strained quantum wells," *Appl. Phys. Lett.*, vol. 65, no. 15, pp. 1886–1887, Oct. 1994, doi: 10.1063/1.112878.

[30] W.-P. Hong and S.-H. Park, "Optical anisotropy in type-II (110)-oriented GaAsSb/GaAs quantum wells," *Solid State Commun.*, vol. 314–315, Jul. 2020, Art. no. 113934, doi: 10.1016/j.ssc.2020.113934.

[31] J.-B. Xia, "Effective-mass theory for superlattices grown on (11N)-oriented substrates," *Phys. Rev. B*, vol. 43, no. 12, pp. 9856–9864, Apr. 1991, doi: 10.1103/PhysRevB.43.9856.

[32] A. Niwa, T. Ohtoshi, and T. Kuroda, "Orientation dependence of optical properties in long wavelength strained quantum-well lasers," *IEEE J. Sel. Topics Quantum Electron.*, vol. 1, no. 2, pp. 211–217, Jun. 1995, doi: 10.1109/2944.401199.

[33] R. Tao et al., "Impact of quantum dots on III-nitride lasers: A theoretical calculation on linewidth enhancement factors," *IEEE J. Sel. Topics Quantum Electron.*, vol. 28, no. 1, Jan./Feb. 2022, Art. no. 1500107, doi: 10.1109/JSTQE.2021.3082162.

[34] I. Vurgaftman, J. R. Meyer, and L. R. Ram-Mohan, "Band parameters for III–V compound semiconductors and their alloys," *J. Appl. Phys.*, vol. 89, no. 11, pp. 5815–5875, Jun. 2001, doi: 10.1063/1.1368156.

[35] Y.-K. Kuo, S.-H. Yen, M.-W. Yao, M.-L. Chen, and B.-T. Liou, "Numerical study on gain and optical properties of AlGaInAs, InGaNAs, and InGaAsP material systems for 1.3-μm semiconductor lasers," *Opt. Commun.*, vol. 275, no. 1, pp. 156–164, Jul. 2007, doi: 10.1016/j.optcom.2007.02.025.

[36] J. Chi, C. Niu, and J. Zhao, "Parameter extraction for quantum well DFB lasers based on 1D traveling wave model," *IEEE Photon. J.*, vol. 14, no. 5, Oct. 2022, Art. no. 1548508, doi: 10.1109/JPHOT.2022.3201578.

[37] X. Li, *Optoelectronic Devices: Design, Modeling, and Simulation*. Cambridge, U.K.: Cambridge Univ. Press, 2009.

[38] Y. C. Yeo, T. C. Chong, M.-F. Li, and W. J. Fan, "Electronic band structures and optical gain spectra of strained wurtzite GaN–AlGaN quantum-well lasers," *IEEE J. Quantum Electron.*, vol. 34, no. 3, pp. 526–534, Mar. 1998.

[39] T. Yamanaka, Y. Yoshikuni, K. Yokoyama, W. Lui, and S. Seki, "Theoretical study on enhanced differential gain and extremely reduced linewidth enhancement factor in quantum-well lasers," *IEEE J. Quantum Electron.*, vol. 29, no. 6, pp. 1609–1616, Jun. 1993, doi: 10.1109/3.234412.

[40] J. Liu et al., "L-band directly modulated laser for 10G PONs," in *Proc. IEEE Prog. Electromagn. Res. Symp.*, 2016, pp. 2718–2718.

[41] U. Bandelow, R. Hunlich, and T. Koprucki, "Simulation of static and dynamic properties of edge-emitting multiple-quantum-well lasers," *IEEE J. Sel. Topics Quantum Electron.*, vol. 9, no. 3, pp. 798–806, May/Jun. 2003, doi: 10.1109/JSTQE.2003.818343.